

Sideband attraction via internal resonance in a multimode membrane as a mechanism for frequency combs

Mengqi Fu ^{1,*} Orjan Ameye ^{1,*} Fan Yang ¹ Jan Košata ² Javier del Pino ¹ Oded Zilberberg ^{1,†} and Elke Scheer ^{1,‡}

¹Department of Physics, University of Konstanz, 78457 Konstanz, Germany

²Institute for Theoretical Physics, ETH Zurich, 8093 Zurich, Switzerland



(Received 21 September 2024; accepted 16 July 2025; published 6 August 2025)

We explore self-induced parametric coupling between a driven (low frequency) and an undriven (high frequency) mode, also called internal resonances, in a membrane micromechanical system. Specifically, we focus on the formation of a limit cycle (LC) manifesting as a phononic frequency comb. As the LC formation involves a Hopf bifurcation, we developed a dedicated pump-noisy-probe technique to investigate which mechanical sidebands merge at the bifurcation. We reveal that the sideband of the driven lower mode is up-converted via a cross-Duffing nonlinearity to hybridize with the undriven high mode. When the up-conversion is initially red detuned relative to the high mode, significant squeezing and bimodality in the high mode occurs. Crucially, only when the up-converted sideband is initially blue detuned relative to the high mode, the sideband is attracted to the high mode and merges to form the Hopf bifurcation. This process delineates the microscopic origin of frequency comb formation. Our study reveals a key instability mechanism in driven nonlinear systems with implications for advanced sensing technologies and phononic metamaterials.

DOI: [10.1103/3mtc-j9r9](https://doi.org/10.1103/3mtc-j9r9)

I. INTRODUCTION

Nonlinear systems are prevalent across physical, biological, and engineering domains. They exhibit rich phenomena, including bifurcations, self-sustained limit cycles (LCs), and chaos [1,2]. Unlike linear systems, where the normal modes are independent, nonlinear systems allow them to interact and exchange energy. When two modes meet internal resonance (IR) conditions, where frequencies approach specific integer ratios, energy exchange becomes resonant [3]. These interactions often involve parametric coupling mediated by three-wave or four-wave mixing [4–6], with an external drive enhancing the coupling strength and enabling dynamic control of interactions. Nonlinear dynamics lead to multiple nonequilibrium stationary solutions (NESSs) and associated phase space topologies with bifurcations driving phase transitions [7,8]. On top of the NESSs, nonlinear coupling can also induce LCs [9–13]. The LCs are often heralded by Hopf bifurcations, where excitations become unstable via gain in the system. The prevalence of LCs in various fields, such as neural rhythms, fluid flow transitions, disease outbreaks, business cycles, and pattern formation [14–17], makes it crucial to study the behavior of excitations around LCs. Nano- and micromechanical systems lend themselves for studying such effects, since their dynamics are prominently nonlinear,

a consequence of surface forces overtaking volume forces at small length scales [18,19].

In this work, by monitoring the response of a mode-coupled nanomechanical system by pump-noisy-probe (PNP) spectroscopy—beyond its conventional use in single-mode dynamics [20–23], we provide insight into NESS under IR conditions. The behavior of NESS is echoed in the dynamics of sidebands around fixed points, with telltales of squeezed fluctuations along with overdamped-to-underdamped transitions and instabilities [24], yielding under certain conditions the formation of a frequency comb. Although the formation of a frequency comb in IR scenarios has been reported before [9–12], the microscopic mechanism for its onset has not been identified so far, mainly due to lack of experimental evidence on which a mechanistic theoretical model could build. As we show, this gap is closed by the so far unexplored usage of PNP under IR conditions as well as by the systematic analysis of sideband structures as a function of the drive frequency.

II. EXPERIMENTAL SETUP AND RESULTS

Our experimental setup, depicted in Fig. 1(a), is built upon a suspended almost square-shaped silicon nitride (SiN) membrane framed by a silicon chip that is attached to a piezo disk. It supports kilohertz-frequency flexural vibration modes labeled with wave numbers (n, m) , where n and m count the deflection extremes along the x and y directions. To excite these modes, a single harmonic alternating current (AC) electrical voltage $V_1(t) = V_1 \sin(\omega_d t)$ is applied across the piezo at a frequency $f_d \equiv \omega_d/2\pi$ near the natural frequency $f_1 = \Omega_1/(2\pi) = 576$ kHz of the $(1, 3)$ mode, called m_1 henceforth. The membrane vibrates along the z axis perpendicular to an externally applied magnetic field; see Fig. 1(a). This setup, introduced in Ref. [21], linearly transduces mechanical motion into readout voltage signals via electromagnetic induction; see

*These authors contributed equally to this work.

†Contact author: oded.zilberberg@uni-konstanz.de

‡Contact author: elke.scheer@uni-konstanz.de

Published by the American Physical Society under the terms of the Creative Commons Attribution 4.0 International license. Further distribution of this work must maintain attribution to the author(s) and the published article's title, journal citation, and DOI.

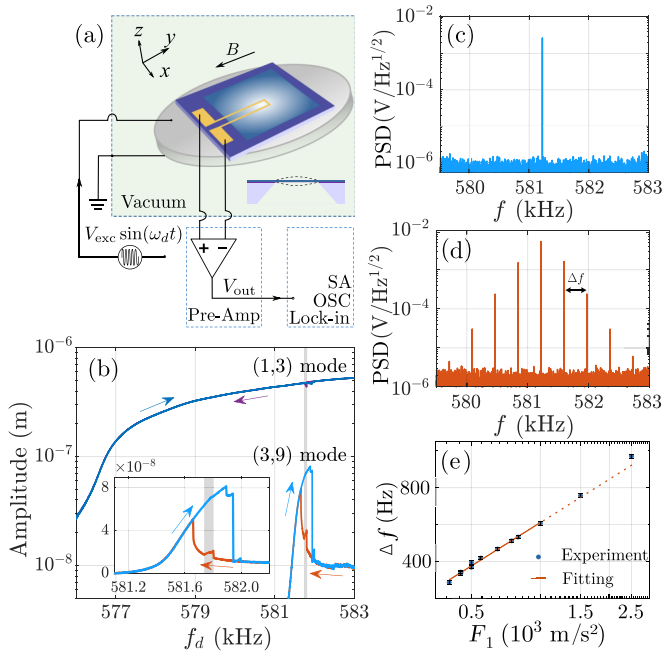


FIG. 1. Setup and its NESS. (a) Schematic drawing of the SiN membrane resonator (cross section in the inset) and the on-chip detection scheme utilizing an inductive probe scheme with a detection electrode patterned on the surface of the membrane. The vibrating membrane resonator generates an induction voltage within a uniform magnetic field, with the output signal being proportional to the vibrational amplitude beneath the electrode. The output signal is measured by a lock-in amplifier, a spectral analyzer (SA), and an oscilloscope (OSC). (b) Amplitude response of the membrane resonator at the drive frequency f_d and its third harmonic $3f_d$, as f_d is swept upward (blue arrows) and then downward (purple and orange arrows). The gray line marks the position where PSDs in panels (c) and (d) are measured. Inset: Zoom-in on the response of the (3, 9) mode (m_2). (c) PSD around the f_d peak along the upward sweep. (d) Same as panel (c) along the down sweep, marking the formation of a frequency comb with a frequency space Δf . All measurements were performed in vacuum and at room temperature. Here, $V_1 = 100 \text{ mV}$. (e) Measured dependence of Δf on F_1 .

Fig. 1(a). For further details on sample fabrication, setup, and data acquisition, we refer to the Appendixes A and B, as well as Refs. [21,25–27].

In Fig. 1(b), we show the amplitude response at the drive frequency f_d and its third harmonic $3f_d$ for up and down frequency sweeps. The amplitude of m_1 follows along the high-amplitude branch of a Duffing-shaped response. Notably, we observe motion not only in the driven mode m_1 but also in the (3, 9) mode, denoted by m_2 henceforth, with natural frequency $f_2 = \Omega_2/2\pi = 1.738 \text{ MHz}$. Note that $f_2 \approx 3f_1$, indicative of an IR. The m_2 is internally driven by m_1 's high-amplitude motion, which induces a Duffing-shaped response in m_2 : Both its high- and low-amplitude branches appear along a hysteretic response relative to the up and down sweeps. We also measure the power spectral density (PSD) along the sweep; see Figs. 1(c) and 1(d). The PSD around the high-amplitude branch of m_2 displays a single peak at f_d . Strikingly, during the down sweep along the low-amplitude branch of m_2 , the PSD suddenly exhibits a frequency comb

around f_d , with a spacing of approximately $\Delta f = 380 \text{ Hz}$ between adjacent sidebands. This spacing does not result from simple algebraic combinations or harmonics of the system's natural frequencies, suggesting a mechanism more complex than resonant wave mixing [28]. The PSD of the frequency combs can be tuned by adjusting f_d while approximately maintaining their spacing Δf . The free spectral range of the comb is strongly dependent on the input power, with Δf showing a logarithmic dependence on the effective force F_1 of the input power, as shown in Fig. 1(e). $F_1(t) \propto V_1(t)$ represents the generalized external force acting on m_1 as controlled by the applied AC voltage, where $F_1 \sim 10^3 \text{ m/s}^2$ corresponds to $V_1 \sim 200 \text{ mV}$. This simple dependence of Δf on V_1 makes the control of Δf practical.

Next, we apply the PNP scheme [20,21,23] to link the system's linear response with the frequency comb formation and observe the microscopic mechanism behind it. The PNP involves driving the system to a NESS using a drive $V_1(t)$ as before, complemented by a weak white-noise drive, with root mean square voltage $V_{\text{rms}} = 100 \text{ mV}$ and bandwidth 2.5 MHz . The latter probes the linear response, indicating the system's eigenmodes and appearing as small sideband excitations, around the NESS in the frequency spectra under different f_d [21]. This approach enables simultaneous access to all frequency components in the spectra, allowing us to resolve the formation of the comb and track the transition from NESS to LC.

The obtained PNP spectra around $f_j \in (f_d, 3f_d)$ are presented in Fig. 2 for an up sweep [(a) and (b)] and a down sweep [(c) and (d)] of f_d . The PNP spectra show, in this case, up to four sidebands around each f_j , two blue and two red detuned, with symmetric frequencies and asymmetric PSD. As f_d is swept upward, we observe an avoided crossing between the sidebands, followed by increased visibility of all four sidebands. A jump $\textcircled{I} \rightarrow \textcircled{II}$ in the PNP response marks the transition between the high- and low-amplitude NESSs in m_2 . Along the down sweep, we observe the sideband signature of the transition $\textcircled{III} \rightarrow \textcircled{IV}$, where the low m_2 amplitude NESS becomes unstable and the frequency comb regime appears. The comb at \textcircled{IV} , in the PNP, has the same PSD as in Fig. 1(d), marking a robustness to the added noise. At lower detuning, the frequency comb dissolves into \textcircled{V} . Eventually, the jump $\textcircled{V} \rightarrow \textcircled{VI}$ marks the transition from the low- to the high-amplitude NESS of m_2 .

III. MODEL AND METHOD

To describe the experimental features in Figs. 2(a)–2(d), we apply linear response theory on top of the stationary motion at ω_d and the up-converted stationary motion at $3\omega_d$. Starting from the membrane's stress-strain equations [29], we truncate the model to describe the dynamics of the modes m_1 and m_2 . Their displacement x_1, x_2 then obeys (see Appendix F)

$$\begin{aligned} \ddot{x}_1 + \tilde{\Omega}_1^2(x_1)x_1 + \tilde{\Gamma}_1(x_1)\dot{x}_1 + 3\xi x_1^2 x_2 + \zeta x_1 x_2^2 &= F_1(t), \\ \ddot{x}_2 + \tilde{\Omega}_2^2(x_2)x_2 + \tilde{\Gamma}_2(x_2)\dot{x}_2 + \xi x_1^3 + \zeta x_1^2 x_2 &= 0. \end{aligned} \quad (1)$$

Here, $\tilde{\Omega}_j(x_j)$ and $\tilde{\Gamma}_j(x_j)$ represent the renormalized natural angular frequencies and damping rates for mode j ,

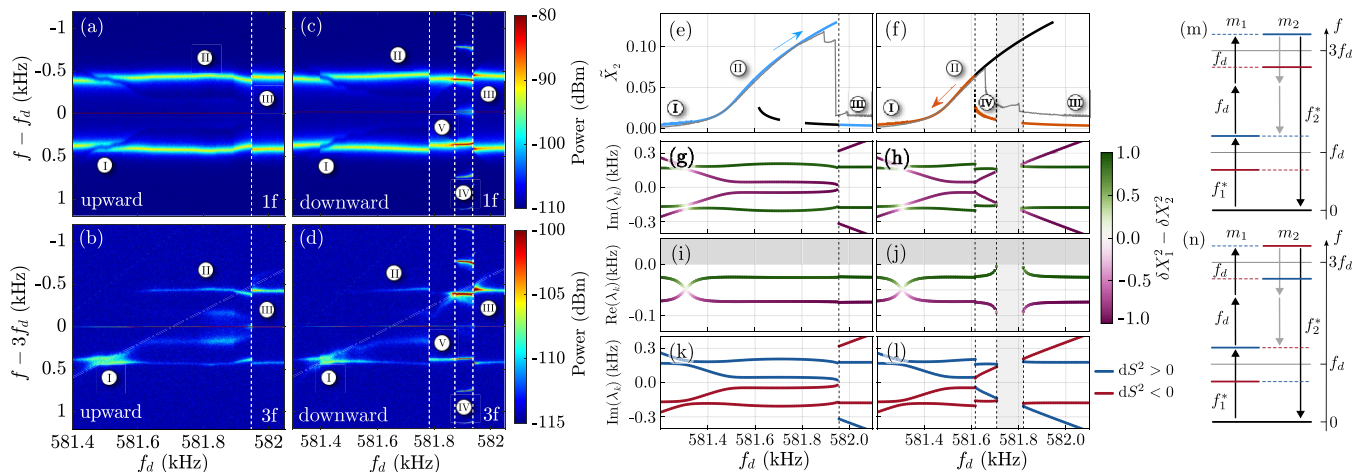


FIG. 2. PNP response. (a) and (b) Sidebands around f_d and $3f_d$ along an up sweep of f_d . (c) and (d) Same as before for a down sweep of f_d . Dashed vertical lines indicate bifurcations. Significant phenomena in the response are labeled by markers ①–⑤. (e) and (f) Theory-predicted stationary amplitude response [cf. Eq. (1)] of m_2 for the up and down sweeps, respectively. Experimentally observed solutions appear in color and others in black. The experimental amplitude response is shown in gray. (g)–(l) Corresponding excitation eigenvalues on top of the sampled stationary solution [cf. Eq. (3)]. (g) and (h) Imaginary part of the eigenvalues colored by the state’s weight in m_1 relative to m_2 . (i) and (j) Real part of the eigenvalues with same coloring as in panels (g) and (h). Panels (k) and (l) correspond to panels (g) and (h), but colored by the symplectic norm of the eigenstates. (m) Laboratory-frame resonant four-wave mixing diagram of the avoided crossing in ①, where $f_1^* = f_d + \text{Im}(\lambda_1)$ and $f_2^* = 3f_d + \text{Im}(\lambda_2)$. (n) Same as panel (m) describing the level attraction where an absorbing and an emitting sideband engender the LC formation.

respectively. Defined in terms of natural angular frequencies Ω_j and linear dampings Γ_j , they read $\tilde{\Omega}_j(x_j) = \sqrt{\Omega_j^2 + \beta_j x_j^2}$ and $\tilde{\Gamma}_j(x_j) = \Gamma_j + \eta_j x_j^2$, where β_j and η_j denote the strengths of the intrinsic Duffing nonlinearity and the nonlinear damping coefficient, respectively. The coefficients ξ and ζ in Eq. (1) quantify the strengths of the relevant cross-Duffing processes that couple the modes. Mechanical parameters are extracted by fitting their linear and weakly nonlinear amplitude responses as well as from ringdown measurements (see Appendix B).

Assuming that each mode mostly responds at the drive frequency nearest its natural frequency, we employ a rotating ansatz [24,29,30]:

$$x_1 = \frac{\alpha_1}{\sqrt{2}} e^{i\omega_d t} + \text{c.c.}, \quad x_2 = \frac{\alpha_2}{\sqrt{2}} e^{i3\omega_d t} + \text{c.c.}, \quad (2)$$

where ω_d is close to Ω_1 , making $3\omega_d$ close to Ω_2 , α_j are slow complex amplitudes, and c.c. stands for complex conjugation. Plugging the ansatz into Eq. (1) and averaging over the slower oscillation period $2\pi/\omega_d$, we obtain time-independent equations of motion (EOMs) for the slow amplitudes, $\dot{\alpha} = \mathbf{F}(\alpha)$, where $\alpha = (\alpha_1, \alpha_2)^T$ (see Appendix F). Using HarmonicBalance.jl [30], we find the system’s stationary solutions $\tilde{\alpha}_n$, where $\mathbf{F}(\tilde{\alpha}_n) \equiv 0$ where n iterates over all solutions. Hence, we find a variety of NESSs as a function of ω_d ; see Figs. 2(e) and 2(f). Performing a numerical up and down sweep in ω_d , yield a good agreement with the experimentally-observed stationary amplitudes. Note that LCs are not captured as a NESS under this ansatz [13]. To describe the PNP sideband spectra, we derive linearized EOMs around each NESS, $\tilde{\alpha}_n$, of Eq. (2):

$$i \begin{pmatrix} \delta \dot{\alpha}_n \\ \delta \dot{\alpha}_n^* \end{pmatrix} = \begin{pmatrix} \mathcal{A}^n - i\frac{\Gamma}{2} & \mathcal{B}^n \\ -\mathcal{B}^{n*} & -\mathcal{A}^{n*} - i\frac{\Gamma}{2} \end{pmatrix} \begin{pmatrix} \delta \alpha_n \\ \delta \alpha_n^* \end{pmatrix}, \quad (3)$$

for small deviations, $\delta \alpha_n \equiv \alpha - \tilde{\alpha}_n = (\delta \alpha_1, \delta \alpha_2)^T$. The matrix \mathcal{A}^n captures the sideband frequencies and their nonlinear shifts (diagonal terms), as well as coupling between the sideband modes at ω_d and $3\omega_d$ (off-diagonal terms). The matrix \mathcal{B}^n describes single-mode squeezing (diagonal terms) and two-mode squeezing (off-diagonal terms). The matrix $\Gamma = \text{diag}(\Gamma_1, \Gamma_2)$ accounts for dissipation. Note that the diagonal terms shift due to the intrinsic Duffing nonlinearities of each mode, whereas the off-diagonal terms shift due to cross-Duffing interactions; cf. explicit expressions (see Appendixes F and G). The eigensolutions of Eq. (3) take the form $\mathbf{w}_k e^{\lambda_k t}$, with $k = 1, \dots, 4$, eigenmodes \mathbf{w}_k , containing complex amplitudes (eigenvector) $\mathbf{w}_k = (c_k^{\alpha_1}, c_k^{\alpha_2}, c_k^{\alpha_1^*}, c_k^{\alpha_2^*})$, and complex eigenvalues λ_k . The NESS subscript n is omitted for clarity, implicit throughout. Each eigenvalue λ_k corresponds to a sideband oscillation at a frequency $\text{Im}(\lambda_k)$, representing the eigenfrequencies of the eigenmodes in the rotating frame, and damping $\text{Re}(\lambda_k)$ in the rotating frame (2). In Figs. 2(g)–2(j), we plot the obtained λ_k for the sampled NESS in the experiment. We color the eigenvalues with the relative contribution of m_1 and m_2 to the corresponding eigenmode calculated by Eq. (3), using $\delta X_k^1 - \delta X_k^2$ with $\delta X_k^j = \sqrt{|c_k^{\alpha_j}|^2 + |c_k^{\alpha_j^*}|^2}$.

The decisive quantity for the formation of a frequency comb is the symplectic norm, $dS_k^2 = \sum_j [c_k^{\alpha_j} (c_k^{\alpha_j})^* - c_k^{\alpha_j^*} (c_k^{\alpha_j})]$ (see Appendix G3), which is shown in Figs. 2(k) and 2(l). The symplectic norm captures whether the combined effect of mode coupling and squeezing yields energy absorbing ($dS_k^2 > 0$) or emitting ($dS_k^2 < 0$) characteristics for each eigenmode \mathbf{w}_k . This distinguishes the eigenmodes in behavior as a conventional harmonic oscillator potential (HO; $dS_k^2 > 0$) sideband or an inverted harmonic oscillator

potential (IHO, $dS_k^2 < 0$) sideband relative to the rotating frame [31,32]. One also can understand this distinction as a sideband motion (back to the time domain) being amplified ($dS_k^2 < 0$) or attenuated ($dS_k^2 > 0$) in amplitude, or being faster or slower than the respective rotating frame at frequency ω_d or $3\omega_d$ [7]. Since PNP probes all excitations in the laboratory frame, we rotate the sideband modes back to the laboratory frame using the inverse of Eq. (2). This results in four spectral sidebands, around both ω_d and $3\omega_d$, with an amplitude imbalance indicative for mode squeezing [20], and spectral widths that account for the lifetimes, matching the experimental results in Figs. 2(a)–2(d).

IV. DISCUSSION

We first apply our theory to the up sweep experiment. As the system climbs the high-amplitude Duffing state of m_1 , the frequencies of its respective sidebands blueshift due to the hardening Duffing nonlinearity. In the strongly driven regime, m_1 's amplitude saturates due to the nonlinearity, slowing down the frequency renormalization of m_1 's sidebands [33] (see Appendixes F and G). This manifests as a flat dependency of the sideband frequencies in the rotating frame; see Fig. 2. As it is only weakly driven, m_2 's sidebands align with its natural frequency f_2 . Hence, in the rotating frame, its sideband frequencies develop linearly with detuning. When the sidebands of the two modes approach each other, they exhibit an avoided crossing ① due to diagonal terms of \mathcal{A}^n having the same phase, i.e., both resonators having a positive dS_k^2 and renormalized natural frequency $\tilde{\Omega}_j/2\pi$, comparing with f_d or $3f_d$, respectively. The observed level repulsion produces signatures akin to parametric coupling under three-wave mixing [4–6,34–37]. However, it arises from stimulated four-wave mixing between m_1 and m_2 in Eq. (1) in the laboratory frame, as exemplified in Eq. (3); this occurs as the up-converted sideband of m_1 approaches Ω_2 from a red-detuned direction; see Fig. 2(m). Note that the avoided crossing occurs when the sidebands of type HO or IHO, interact with the same type HO or IHO, respectively [cf. Figs. 2(k)–2(m)]; only then is the direct coupling dominant in Eq. (3).

Far above the avoided crossing (Ⓜ in Fig. 2), both modes reach high-amplitude saturation. As a result, the sideband response of m_2 becomes mostly independent of the detuning, and direct coupling plays no significant role. In this region, the appearance of PNP sidebands with symmetric frequencies around ω_d and $3\omega_d$ indicates dominant squeezing via the \mathcal{B}^n term [20,38].

At even higher detuning, both sidebands of m_2 move toward $\text{Im}(\lambda_k) = 0$ in the rotating frame. This softening signals that m_2 's sidebands become resonant with the up-converted pump at $3\omega_d$. As a consequence, the system becomes unstable and transitions from a NESS with a high amplitude to a low amplitude in m_2 . After this transition into Ⓜ, the system is in a similar state as where the upward sweep started: m_1 remains in its high-amplitude Duffing branch and m_2 is in its low-amplitude state. Crucially, however, the m_2 's HO sideband is now lower in frequency than the up-converted pump in $3\omega_d$, and correspondingly dS_k^2 of that m_2 sideband is inverted in Ⓜ relative to ①—it has a negative frequency in the up-converted

rotating frame. Thus, the upper sideband of m_2 becomes an IHO in Ⓜ; see Figs. 2(h) and 2(l). Apart from this inversion, the onset of the down sweep in Ⓜ mirrors the initial conditions of the up sweep experiment: m_2 's eigenfrequency remains linearly susceptible to the detuning, while m_1 shows squeezing signatures [cf. sideband asymmetry in Figs. 2(c) and 2(d)], which are independent of the detuning.

As the down sweep progresses, the modes's eigenfrequencies come closer. Unlike the anticrossing in ①, in Ⓜ the sign of dS_k^2 flips for the m_2 eigenmodes, and thus the one sideband of type HO and one of type IHO interact with each other [cf. Figs. 2(k), 2(l), and 2(n)], fostering an energy exchange among them. This mechanism destabilizes the NESS, triggering LC oscillations that appear as a frequency comb in the PSD [cf. Figs. 1(d), 2(c), and 2(d)]. Indeed, this level attraction precipitates a Hopf bifurcation, where the eigenmode's lifetime vanishes but its frequency remains finite ($\text{Im}(\lambda_k) \neq 0$) [39,40], as shown in Figs. 2(h) and 2(j). Contrary to the resonance behavior in ①, the diagonal elements of \mathcal{A}^n have an opposite phase, creating a feedback loop between the sideband oscillations that destabilizes m_1 [cf. Figs. 2(j) and 2(n)]. Namely, in the laboratory frame, vibrations in m_1 are up-converted to m_2 via cross-Duffing nonlinearity and down-converted back to the resonant sideband of m_1 . In the rotating frame, this instability formally resembles that caused by mode gap closure due to ultrastrong parametric coupling [6,10,41,42]. Continuing the down sweep, the LC collapses back into ②, stabilizing both m_1 and m_2 . As sidebands of m_2 approach resonance with the up-converted pump again, m_2 enters its high-amplitude Duffing state, flipping the sign of dS_k^2 .

V. CONCLUSION

In conclusion, we uncover how internal resonance drives the transition from steady-state vibrations to frequency comb dynamics in a nanomechanical resonator. The emergence and evolution of sideband structures reveals the transition from a nonlinear steady state to a limit cycle and captures the onset and progression of frequency comb formation in the intermediate regime. Through these direct experimental results and in-depth theoretical modeling, we revealed the microscopic origin of the LC formation in parametrically coupled nonlinear systems. Two conditions have to be fulfilled for the LC formation: First, the gap between sidebands closes in the PNP spectra via resonant four-wave mixing. Second, the type of sidebands (energy absorbing or emitting) that hybridize is decisive, i.e., whether the sidebands repel or attract. This mechanism of ultrastrong coupling between sidebands as a source for generating LCs mimics the onset of ultrastrong coupling seen in light-matter systems [43] and hence carries over beyond IR scenarios. Our study opens avenues for exploring the fundamental physics of multimode resonator networks, with implications for metamaterial science, sensing technologies, and neuromorphic computing including quantum implementations.

ACKNOWLEDGMENTS

The authors thank J. Boneberg for help with the experimental setups. We are indebted to J. S. Ochs, E. M. Weig, G. Rastelli, P. Leiderer, and W. Belzig for fruitful discussion

and comments about the work. The authors acknowledge the use of the experimental equipment and the expert support provided by the nano.lab at the University of Konstanz. The authors gratefully acknowledge financial support from the Swiss National Science Foundation (SNSF) through the Sinergia Grants No. CRSII5 177198/1 and No. CRSII5_206008/1, and the Deutsche Forschungsgemeinschaft (DFG, German Research Foundation) through SFB 1432 (Project ID 425217212) and Project IDs 449653034 and 510766045. This work was also supported by the Major Program in Digital Intelligence, Chongqing (Grant No. 20240204), and the Technology Innovation and Application Development Program, Chongqing (Grant No. CSTB2025TIAD-qykjggX0439).

DATA AVAILABILITY

The data that support the findings of this article are not publicly available. The data are available from the authors upon reasonable request.

APPENDIX A: SAMPLE FABRICATION AND VIBRATION DETECTION METHOD

The SiN membranes are fabricated from a 0.5 mm thick commercial (100) silicon wafer. Both sides of the silicon substrate are coated with ~ 500 nm thick low-pressure chemical vapor deposited SiN. The membrane is fabricated on the front side. The backside layer serves as an etch mask. Laser ablation is used to open an etch mask with a typical size of $1.5 \times 1.5 \text{ mm}^2$. Using anisotropic etching in aqueous potassium hydroxide (KOH), a hole is etched through the openings of the mask. After the KOH solution reaches the topside layer, the etching stops and a SiN membrane is formed, supported by a massive silicon frame. The membrane is approximately rectangular in shape ($542 \times 524 \mu\text{m}^2$ lateral size) and supports vibrational modes characterized by numbers (n, m) indicating the number of deflection maxima along the directions x and y .

To detect the mechanical vibration of the SiN membrane, thin aluminum leads (~ 27 nm) are fabricated on the upper surface of the suspended membranes, as well as on the Si frame by standard electron beam lithography and electron beam evaporation. The chip with approximately $10 \times 10 \text{ mm}^2$ lateral size carrying the membrane is glued to a piezo disk of 12 mm diameter and 1 mm thickness using a two-component adhesive; see Fig. 3.

For the acquisition of the data in the main text, we used the magnetic induction method to characterize the amplitude of the membrane, as depicted in Fig. 1(a). The device is placed in a vacuum chamber with a pressure of $p = 10^{-6}$ mbar at room temperature and subject to an in-plane magnetic field of flux density amplitude B . The Al electrode deposited onto the membrane builds the detection electrodes perpendicular to the magnetic field and their peripheral leads parallel to the magnetic field. For the sample used in this manuscript, two detection electrodes are located close to the center and at a corner of the membrane, respectively, and both have the length of $L = 30 \mu\text{m}$.

When the membrane vibrates, the magnetic flux through the area enclosed by the detection electrode and the peripheral leads changes, and thus a potential difference is generated

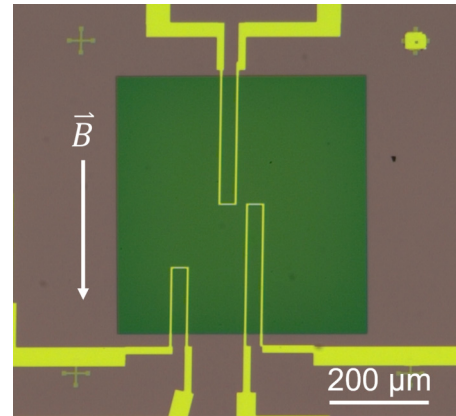


FIG. 3. Optical micrograph (top view) of the membrane resonator. Green area: free-standing membrane; brownish area: SiN on top of Si. Yellow lines: three independent electrodes. All measurements reported here have been recorded with the rightmost electrode pair. The arrow indicates the direction of the applied magnetic field.

across the electrodes on the membrane. The generated potential difference is first fed to the two input ports of a differential preamplifier to be converted into a single-ended output voltage (V_{out}) amplified by a factor (G_{diff}). The use of the differential preamplifier can efficiently suppress common-mode noise (such as the noise generated in the wires and from the vibration of the sample stage). The vibration of the membrane part under the peripheral leads does not contribute to V_{out} because the peripheral leads are parallel to the magnetic field. Therefore, the vibration velocity (v) of the membrane part under the detection electrode is linearly related to V_{out} by a factor of $(G_{\text{diff}}BL)^{-1}$, where $B = 0.45$ T. Hence, when the membrane is driven by the piezo with the excitation

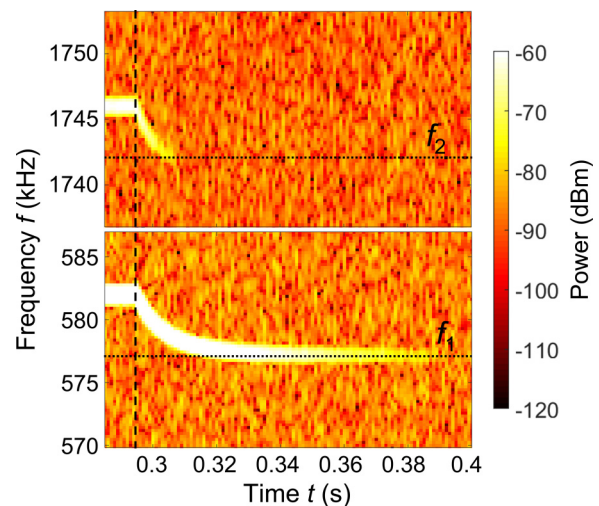


FIG. 4. Ringdown measurement under $V_1 = 100$ mV and $f_d = 582$ kHz. The color encodes the intensities of the response in the frequency ranges around f_d and $3f_d$. The drive power is switched off at the dashed vertical line. Then, the amplitude decreases and the frequencies develop toward the natural frequencies f_1 and f_2 , indicated by the horizontal lines corresponding to the m_1 and m_2 modes, respectively.

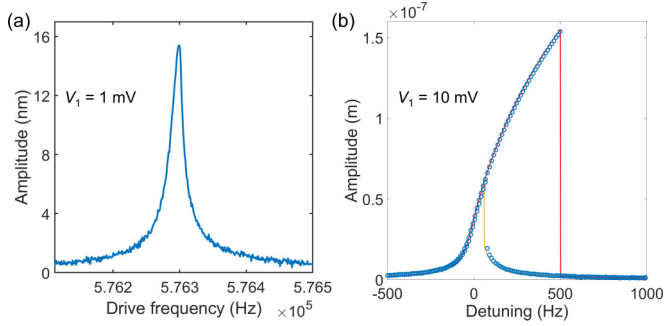


FIG. 5. Linear and nonlinear frequency responses of m_1 of the SiN resonator driven with (a) $V_1 = 1$ mV and (b) $V_1 = 10$ mV. Blue symbols: experimental; red (yellow) line: fit with Duffing model for the up sweep (down sweep).

voltage of V_1 at the frequency of $\omega_d = 2\pi f_d$, the velocity is $v(t) = A\omega_d \cos(\omega_d t)$ and the real vibration amplitude (A) at the position of the detection electrode can be easily calculated by

$$A = \frac{V_{\text{out}}}{BL\omega_d G_{\text{diff}}}. \quad (\text{A1})$$

APPENDIX B: CHARACTERIZATION OF MECHANICAL PROPERTIES OF THE MEMBRANE

The Young's modulus E and the residual stress σ of the SiN membrane used in the present work are measured as $E = 213$ GPa and $\sigma = 0.1$ GPa, respectively, extracted from the dispersion curve of the bending waves; for details, see our previous work [21]. As shown in Fig. 1(b), a flexural mode shows a response at f_d from 576 to 583 kHz and another flexural mode is coupled into the vibration by 1:3 internal resonance and a shark-fin-shaped frequency response appears at $3f_d$ ($f_d = 581$ – 582 kHz). To determine which flexural mode it is, a ringdown measurement is performed. V_1 is swept up to 582 kHz where the amplitude response at $3f_d$ is large and then V_1 is switched off (indicated by the white dashed line in Fig. 4). The vibration trace during the ringdown measurement is captured and converted into frequency spectra by fast Fourier transformation, as shown in Fig. 4. After the drive power is switched off, the amplitude of the vibration reduces

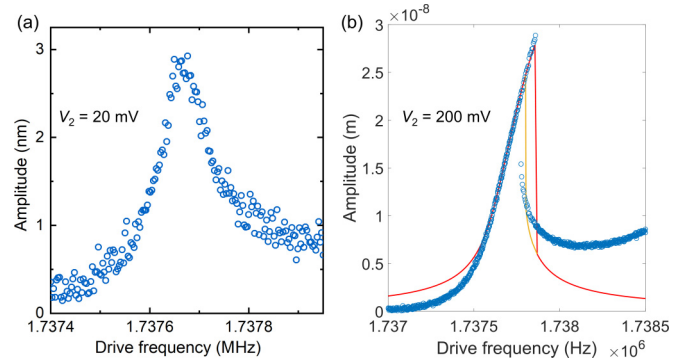


FIG. 6. Linear and nonlinear frequency responses of the m_2 mode driven directly with AC electric voltage: (a) $V_2 = 20$ mV and (b) $V_2 = 200$ mV. In panel (b), the measured amplitudes are plotted as blue dots, and the theoretical calculation of the Duffing model is plotted as red (up sweep) and yellow (down sweep) lines. The asymmetry observed in panel (a) and the deviation between the experimental data and the Duffing-fitted curves well below the natural frequency and above the dropping points are primarily attributed to the excitation of another mode (either a system mode or another membrane mode with low Q factor) with a natural frequency similar to that of the (3, 9) mode. The vibration amplitude of this additional mode introduces a background to the frequency response of the (3, 9). Since the amplitude of this background is significantly lower than the vibration amplitude of the (3, 9) mode, its impact on the fitting is neglected.

and the frequencies decrease until they finally saturate at the natural frequencies of these modes, enabling us to identify the modes excited at f_d and $3f_d$ in Fig. 1(b) as the (1, 3) (m_1) and (3, 9) (m_2) modes, respectively.

We determined the mechanical parameters of the two driven modes by fitting their linear and weakly nonlinear amplitude responses in Figs. 5 and 6. The extracted parameters are also summarized in Table I. Note that natural frequencies with the same index ratio, e.g., (3, 9) and (1, 3), are not exact integer multiples of each other due to nonlinear factors such as the bending nonlinearity [26]. In our experiments, temperature drifts have been observed to induce frequency shifts on the order of several hundreds of Hz/K [25]. The temperature in the laboratory may vary by a couple of K. Thus, the absolute

TABLE I. Comparison of experimental and theoretical parameters for m_1 and m_2 . Note that the natural frequencies are temperature dependent. The indicated uncertainty denotes the range over which they vary upon a laboratory temperature change of two degrees.

Parameter	Flexural mode	Experiment	Theory
Natural frequency f (kHz)	m_1	$\approx 576 \pm 3.5$	576.635
	m_2	$\approx 1738 \pm 10.5$	1744.375
Damping rate $\Gamma/2\pi$ (Hz)	m_1	14 ± 1	14.2
	m_2	80 ± 3	85.5
Quality factor Q	m_1	$40\,600 \pm 2900$	40\,600
	m_2	$21\,700 \pm 810$	20\,400
Duffing nonlinearity β ($\text{m}^{-2} \text{s}^{-2}$)	m_1	$1.26 \pm 0.05 \times 10^{24}$	1.4×10^{24}
	m_2	$4.2 \pm 0.2 \times 10^{25}$	2.8×10^{25}
Generalized force F (m/s^2)	m_1	500 ± 5	–
Nonlinear damping factor η ($\text{s}^{-1} \text{m}^{-2}$)	m_1	$8.2 \pm 0.5 \times 10^{14}$	8.2×10^{14}
	m_2	$3.8 \pm 0.5 \times 10^{16}$	1×10^{14}

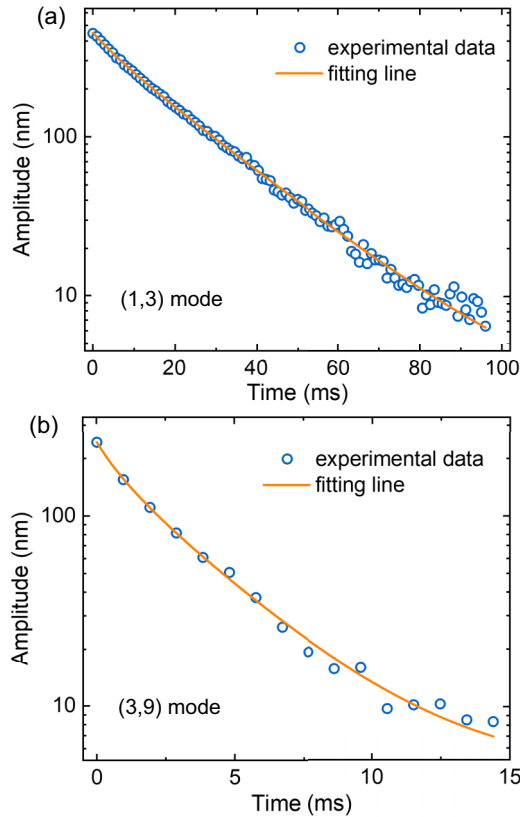


FIG. 7. Ringdown measurements of (a) mode m_1 and (b) mode m_2 . The drive was switched off at $t = 0$. The fits have been calculated with Eq. (B1).

values of the natural frequencies as well as the drive frequency used to excite the flexural modes may vary by a few kHz from measurement to measurement.

To extract the nonlinear damping coefficients of m_1 and m_2 , we excite one flexural mode into its high-amplitude vibration without coupling other flexural modes into the vibration and then turn off the drive to perform ringdown measurements, as shown in Fig. 7. In Figs. 7(a) and 7(b), we show the nonlinear amplitude decays for m_1 and m_2 , respectively. We fit the ringdown curve with [44]

$$X_j(t) = \frac{X_{j,0}e^{(-\Gamma_j t)/2}}{\sqrt{1 + \frac{\eta_j}{4\Gamma_j} X_{j,0}^2 (1 - e^{-\Gamma_j t})}}. \quad (\text{B1})$$

Here, $X_{j,0}$ is the vibration amplitude under the excitation V_j , t is the time after turning off V_j , and $X_j(t)$ is the vibration amplitude as a function of time. The nonlinear damping factors η_j of modes m_1 and m_2 are also indicated in Table I.

APPENDIX C: FREQUENCY SPECTRA AROUND THE DRIVE TONE AND ITS THIRD HARMONIC

Figures 8(a) and 8(b) show line cuts at a fixed driving frequency of $f_d = 581.7$ kHz, corresponding to Figs. 2(a) and 2(b), respectively. The two pairs of sidebands, centered around f_d [Fig. 2(a)] and $3f_d$ [Fig. 2(b)], exhibit an amplitude imbalance.

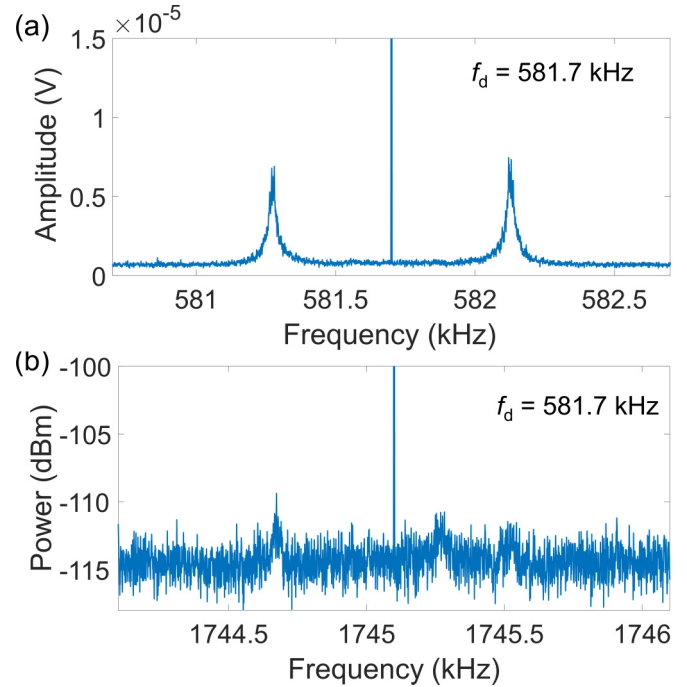


FIG. 8. Frequency spectra around f_d (a) and $3f_d$ (b) in the up sweep of f_d .

APPENDIX D: CLASSIFICATION OF NOISE SIDEBANDS TO THE EXCITED FLEXURAL MODES

Experimentally, the eigenmodes of a flexural mode j can be visualized by the system fluctuations around the NESS ($f = f_d$) as noise sidebands [20,21]. The frequencies of the noise sidebands strongly depend on the vibration amplitude, nonlinearity, and the detuning frequency of the mode [20,21]. When the vibration amplitude of the mode is low, the noise sideband has the same or similar frequency as the natural frequency f_j , and only one noise sideband can be well observed. Instead, when the vibration amplitude of the mode is large, especially entering into the upper branches with relatively large detuning, one eigenmode splits into two eigenmodes and thus a pair of noise sidebands can be observed. In this regime, the frequency spacing between the pair of noise sidebands and f_d becomes relatively constant [33].

Independently of the detailed modeling explained in the main text, we can also assign the sidebands to their respective modes from a purely experimental point of view; i.e., the contribution of the flexural modes to each eigenmode can be experimentally determined and hence each sideband can be assigned as being predominantly arising from a specific flexural mode j . The frequency spacing of the outer pair of sidebands at $f_d = 581.7$ kHz hardly changes (within 100 Hz) with varying f_d in the detuning range shown in Fig. 2. Comparing with the amplitude response of the two coupled modes in Fig. 1(b), this pair of sidebands is assigned to m_1 because the vibration amplitude and detuning of m_1 are large. In contrast, the inner pair of the sidebands at $f_d = 581.7$ kHz presents a significant f_d dependence of the frequency spacing at $f_d = 581$ – 582 kHz. Therefore, they correspond to m_2 .

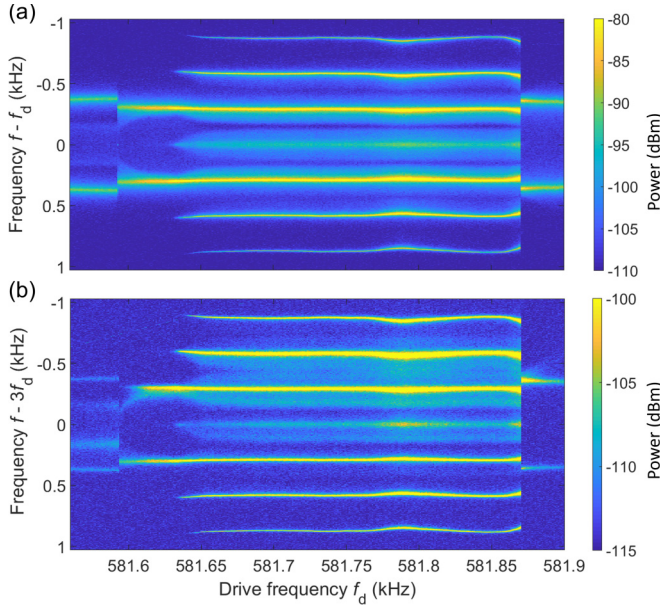


FIG. 9. 2D frequency spectra of the frequency comb excited under $V_1 = 80$ mV. Panels (a) and (b) show the spectra around f_d and $3f_d$, respectively.

In addition, we can also distinguish the eigenmodes of m_1 and m_2 by the bandwidth of the noise sidebands. The linear response of an eigenmode vibrating in the nonlinear regime shows a similar bandwidth as the natural mode [20]. Therefore, the linear response of eigenmodes dominated by m_2 shows a higher damping rate, and the noise sidebands are spectrally broader than those dominated by m_1 . According to the features described above, the comparison of the frequency spectra in Fig. 2(b) with the frequency sweep in Fig. 1(b) confirms the assignment.

APPENDIX E: 2D FREQUENCY SPECTRA UNDER DIFFERENT DRIVE POWER

The generation of the frequency comb has been monitored for different drive powers. Figure 9 shows the 2D frequency spectra of the mechanical vibration under $V_1 = 80$ mV with a PNP measurement. Before and after the frequency comb is excited, two sets of noise sidebands are observed. As in the case of $V_1 = 100$ mV, the frequency comb is excited when the frequencies of these two sets of noise sidebands approach each other. The frequency spacing between the sidebands of the frequency comb is smaller than that observed under $V_1 = 100$ mV. Moreover, traditional phononic frequency combs are driven by nonlinear wave mixing processes, where the sideband intensity increases with the system's oscillation amplitude. In contrast, in our study the pair of the most intense sidebands in the comb arises from the system's limit cycle, and the additional sidebands are harmonics of them. Their amplitude is determined by the shape of the limit cycle trajectory in the four-dimensional phase space, which itself is determined by the cross-coupling strengths of the modes [13,30]. Therefore, increasing the nonlinearity of the system is beneficial for generating a greater number of sidebands in the comb and for pumping more energy into them.

APPENDIX F: DERIVATION OF THE MODEL

1. Rectangular membrane model

Here, we derive the EOMs (1) and (2) of the main text by describing a stretched rectangular elastic membrane under the influence of an external force. This subsection is adapted from Ref. [45]. We are particularly focused on the out-of-plane displacement $w \equiv w(x, y, t)$, which is governed by the field Lagrangian [46,47]

$$\mathcal{L} = \frac{\rho h}{2} \dot{w}^2 - \frac{\bar{\sigma} h}{2} (\nabla w \cdot \nabla w) - \frac{\beta}{4} (\nabla w \cdot \nabla w)^2 - f w. \quad (\text{F1})$$

In the main text, x is used for displacement. However, in this section, we use the w symbol such that x can be used as one of the spatial coordinates. Here, $\bar{\sigma}$ represents the applied stress, ρ is the mass density, and h is the membrane thickness. The nonlinearity coefficient, $\beta = Eh/2(1 - \nu^2)$, depends on Young's modulus E and Poisson's ratio ν . Furthermore, $f \equiv f(x, y, t)$ denotes the external force.

Using the Galerkin discretization method [29], the displacement w can be represented through the normal modes of the linear system (with $\beta = 0$). Each mode is described by a pair of integers $\mathbf{j} = (j_1, j_2)$. For a membrane clamped at the boundaries $x = 0, L_x$ and $y = 0, L_y$, the normal modes take the form

$$\phi_{\mathbf{j}}(x, y) = \sin\left(\frac{j_1 \pi x}{L_x}\right) \sin\left(\frac{j_2 \pi y}{L_y}\right). \quad (\text{F2})$$

These modes serve as a basis to decompose the displacement w , where each mode is factored into its spatial profile $\phi_{\mathbf{j}}(x, y)$ (dimensionless) and its amplitude $u_{\mathbf{j}}(t)$ (having dimensions of length):

$$w(x, y, t) = \sum_{\mathbf{j}} c_{\mathbf{j}}(t) \phi_{\mathbf{j}}(x, y). \quad (\text{F3})$$

This approach is exact when the sum over \mathbf{j} extends to infinity. The corresponding Lagrange's EOMs for each $c_{\mathbf{j}}(t)$ are

$$\begin{aligned} & \left(\rho h \int_S \phi_{\mathbf{j}}^2 dS \right) \ddot{c}_{\mathbf{j}} + \left(\bar{\sigma} h \int_S \nabla \phi_{\mathbf{j}} \cdot \nabla \phi_{\mathbf{j}} dS \right) c_{\mathbf{j}} \\ & + \beta \sum_{\mathbf{k}, \mathbf{l}, \mathbf{m}} C_{\mathbf{jklm}} c_{\mathbf{k}} c_{\mathbf{l}} c_{\mathbf{m}} = \int_S f \phi_{\mathbf{j}} dS, \end{aligned} \quad (\text{F4})$$

where $\int_S dS = \int_0^{L_x} dx \int_0^{L_y} dy$ and $C_{\mathbf{jklm}}$ is a tensor defined by

$$C_{\mathbf{jklm}} = \int_S dS (\nabla \phi_{\mathbf{j}} \cdot \nabla \phi_{\mathbf{k}}) (\nabla \phi_{\mathbf{l}} \cdot \nabla \phi_{\mathbf{m}}). \quad (\text{F5})$$

The linear part of Eq. (F4) provides the natural frequency for each mode:

$$\omega_{\mathbf{j}} = \sqrt{\frac{\bar{\sigma} \int_S \nabla \phi_{\mathbf{j}} \cdot \nabla \phi_{\mathbf{j}} dS}{\rho \int_S \phi_{\mathbf{j}}^2 dS}} = \pi \sqrt{\frac{\bar{\sigma}}{\rho} \left(\frac{j_1^2}{L_x^2} + \frac{j_2^2}{L_y^2} \right)}. \quad (\text{F6})$$

The nonlinear part includes terms involving one or more modes, often referred to as self-nonlinearities or cross-nonlinearities. The self-nonlinearity for each mode, expressed as

$$C_{\mathbf{j}iii} = \frac{9(j_1 L_x)^4 + 2(j_1 j_2 L_x L_y)^2 + 9(j_2 L_y)^4}{64(L_x L_y)^3} > 0, \quad (\text{F7})$$

introduces a cubic term in u_j within Eq. (F4). As a result, each mode exhibits cubic nonlinearity, making the system behave as a Duffing (or Kerr) oscillator.

In this particular case, not all potential mode-coupling terms are present. Using the analytical expressions for ϕ_j , we can identify the nonzero components of the tensor C_{jklm} . From Eq. (F5) and the mode shapes given in Eq. (F2), we encounter two spatial integrals, each involving a product of four cosine functions. For C_{jklm} to be nonzero, these products must result in a constant contribution in both x and y . This condition is satisfied if

$$j_1 \pm k_1 \pm l_1 \pm m_1 = 0 \quad \text{and} \quad j_2 \pm k_2 \pm l_2 \pm m_2 = 0 \quad (\text{F8})$$

hold true for at least one combination of the \pm signs. Evaluating these cross-nonlinearities leads to the EOMs (1) and (2) in the main text.

2. Slow-flow equations

The theoretical model used in the analysis is given by Eqs. (1) and (2). We are interested in the stationary responses of both the m_1 and m_2 modes at the frequency of their respective drives. Therefore, we employ a Floquet expansion in the rotating frame of the drives [cf. Eq. (2)], separating the fast dynamics from the stroboscopic dynamics. We do this with the help of the open-source software package HarmonicBalance.jl [30]. Using the package, we can transform the coupled equations from Eq. (1) into slow-flow equations for the quadratures u_i and v_i :

$$\begin{aligned} \frac{du_1}{dt} = & \left(\frac{\Delta_1}{2} - \frac{3\beta_1}{8\omega_d} X_1^2 - \frac{\zeta}{4\omega_d} X_2^2 - \frac{3\xi}{4\omega_d} Y_{12} \right) v_1 \\ & - \left(\frac{3\xi}{8\omega_d} X_1^2 + \frac{\zeta}{4\omega_d} Y_{12} \right) v_2 + \left(\frac{\eta_1}{8} X_1^2 - \frac{\gamma_1}{2} \right) u_1, \end{aligned} \quad (\text{F9})$$

$$\begin{aligned} \frac{dv_1}{dt} = & \left(\frac{\Delta_1}{2} + \frac{3\beta_1}{8\omega_d} X_1^2 + \frac{\zeta}{4\omega_d} X_2^2 + \frac{3\xi}{4\omega_d} Y_{12} \right) u_1 \\ & + \left(\frac{3\xi}{8\omega_d} X_1^2 + \frac{\zeta}{4\omega_d} Y_{12} \right) u_2 - \left(\frac{\eta_1}{8} X_1^2 + \frac{\gamma_1}{2} \right) v_1 - \frac{F}{2\omega_d}, \end{aligned} \quad (\text{F10})$$

$$\begin{aligned} \frac{du_2}{dt} = & \left(\frac{\Delta_2}{2} - \frac{\zeta}{12\omega_d} X_1^2 - \frac{3\beta_2}{24\omega_d} X_2^2 \right) v_2 \\ & - \frac{\xi}{8\omega_d} Z_1^u v_1 + \left(\frac{\eta_2}{8} X_2^2 - \frac{\gamma_2}{2} \right) u_2, \end{aligned} \quad (\text{F11})$$

$$\begin{aligned} \frac{dv_2}{dt} = & \left(\frac{\Delta_2}{2} + \frac{\zeta}{12\omega_d} X_1^2 + \frac{3\beta_2}{24\omega_d} X_2^2 \right) u_2 \\ & + \frac{\xi}{8\omega_d} Z_1^v u_1 - \left(\frac{\eta_2}{8} X_2^2 + \frac{\gamma_2}{2} \right) v_2, \end{aligned} \quad (\text{F12})$$

with detuning $\Delta_1 = (\omega_d^2 - \omega_1^2)/\omega_d$ and $\Delta_2 = [(3\omega_d)^2 - \omega_2^2]/(3\omega_d)$, nonlinearity β_i , amplitude $X_i = (u_i^2 + v_i^2)^{1/2}$, linear damping γ_i , and nonlinear damping η_i of the i th resonator. The parameters ξ and ζ are the coupling coefficients to the $x_1^3 x_2$ and $x_1^2 x_2^2$ terms, respectively. For convenience, we define $Z_i^u \equiv 3u_i^2 + v_i^2$, $Z_i^v \equiv u_i^2 + 3v_i^2$, and $Y_{12} \equiv u_1 u_2 + v_1 v_2$. The equations can

be easily converted to the coherent fields in the main text by the coordinate transformation $\alpha_1 = \sqrt{(\omega_d/2)}(u_1 - iv_1)$ and $\alpha_2 = \sqrt{(3\omega_d/2)}(u_2 - iv_2)$.

We search for the system's NESS, focusing on the solutions for u_i and v_i , when $\dot{u}_i = \dot{v}_i = 0$. Hence, finding the NESS boils down to identifying the roots of the polynomial system defined by Eqs. (F9)–(F12). To achieve this, HarmonicBalance.jl employs homotopy continuation [48], a technique that guarantees to find all the roots and therefore all the fixed-point NESS (attractors) of the system.

We obtain a good fit with the measured stationary amplitudes $\sqrt{u_1^2 + v_1^2}$ and $\sqrt{u_2^2 + v_2^2}$; see Fig. 2. All figures are generated using the following parameters: natural frequencies $f_1 \approx 576.635$ kHz and $f_2 \approx 1.744375$ MHz, damping rates $\Gamma_1/2\pi = 14.2$ Hz ($Q_1 \approx 40600$) and $\Gamma_2/2\pi = 85.5$ Hz ($Q_2 \approx 20400$), Duffing nonlinearities $\beta_1 = 1.4 \times 10^{24} \text{ m}^{-2} \text{ s}^{-2}$ and $\beta_2 = 2.8 \times 10^{25} \text{ m}^{-2} \text{ s}^{-2}$, and nonlinear damping factors $\eta_1 = 8.2 \times 10^{14}$ and $\eta_2 = 1 \times 10^{14} \text{ m}^{-2} \text{ s}^{-2}$ for m_1 and m_2 , respectively.

APPENDIX G: INTRODUCTION TO LINEAR RESPONSE THEORY FOR RESONATORS

1. Jacobian

In the context of linear response theory, the Jacobian matrix plays a fundamental role in characterizing the system's behavior near NESS. It encodes the linearized dynamics of small perturbations around the steady state. Indeed, considering the EOMs of the system, linearization is performed around the steady state $\tilde{\mathbf{u}}$, which represents the NESS in the phase space. Introducing a small perturbation $\delta\mathbf{u} = \mathbf{u} - \tilde{\mathbf{u}}$, the system's dynamics can be expressed in terms of these deviations as

$$\frac{d\delta\mathbf{u}}{dt} = \mathcal{J}(\tilde{\mathbf{u}})\delta\mathbf{u}, \quad (\text{G1})$$

where $\mathcal{J}(\tilde{\mathbf{u}})$ is the Jacobian matrix evaluated at the steady state $\tilde{\mathbf{u}}$. The Jacobian encapsulates the first-order derivatives of the system's EOMs with respect to the state variables, thus governing the linearized dynamics of the perturbations.

The eigenvalues λ_k of the Jacobian matrix determine the behavior of the perturbations. Since the equation above is a system of first-order ordinary differential equations, the solutions take the form

$$\delta\mathbf{u}(t) \propto e^{\lambda_k t}, \quad (\text{G2})$$

where λ_k are the eigenvalues of \mathcal{J} . The real parts of these eigenvalues, $\text{Re}(\lambda_k)$, dictate the stability of the NESS: If $\text{Re}(\lambda_k) < 0$ for all eigenvalues, the perturbations decay exponentially, ensuring that the steady state $\tilde{\mathbf{u}}$ is stable. Instead, if $\text{Re}(\lambda_k) > 0$ for at least one eigenvalue, the perturbations grow over time, leading to instability. In such a scenario, external disturbances, such as noise or small external drives, can cause the system to deviate significantly from $\tilde{\mathbf{u}}$.

The Jacobian matrix is thus central to linear response theory, offering insights into the stability and transient dynamics of resonator systems near a NESS. By analyzing its eigen-spectrum, one can predict how the system will respond to perturbations and assess the robustness of the steady state under varying conditions.

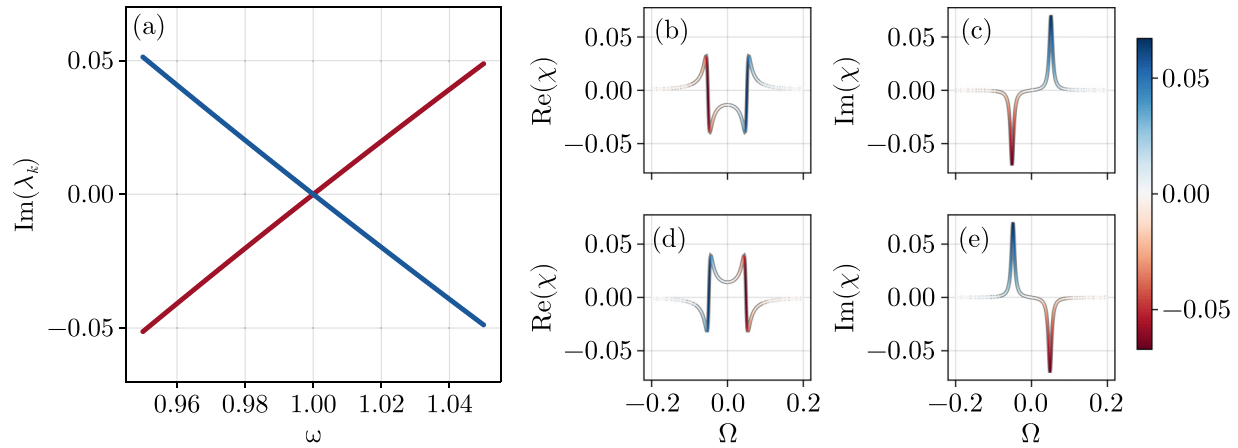


FIG. 10. Linear response of a driven damped harmonic oscillator in the rotating frame. (a) Dependence of the imaginary part of the eigenvalues on detuning, illustrating the linear shift around resonance. The eigenvalues are color coded by the sign of the symplectic norm, i.e., $dS_k^2 > 0$ blue and $dS_k^2 < 0$ red. (b)–(e) The real and imaginary parts of the response function $\chi_{\text{rot}}(\Omega)$ are shown for fixed drive frequencies below and above the natural frequency, highlighting the asymmetry between the absorbing and emitting sidebands. The response function is colored by the contribution difference of the + and – eigenvectors, i.e., $|A_+| - |A_-|$.

2. Linear response in the rotating frame

To analyze the linear response of NESS to an additional oscillatory force, such as weak probes or external noise, we study the behavior of small perturbations $\delta\mathbf{u}$ in the presence of a periodic driving term $\sigma e^{i\Omega t}$, where Ω is the frequency of the external probe. The linear response of these perturbations is governed by Eq. (G1) with the additional drive

$$\frac{d\mathbf{u}}{dt} = \mathcal{J}(\tilde{\mathbf{u}})\delta\mathbf{u} + \sigma e^{i\Omega t}. \quad (\text{G3})$$

To solve this driven linearized equation, we assume a solution of the form $\delta\mathbf{u}_k = A_k(\Omega)\mathbf{w}_k e^{i\Omega t}$, where the eigenvector \mathbf{w}_k is such that $\mathcal{J}(\tilde{\mathbf{u}})\mathbf{w}_k = \lambda_k \mathbf{w}_k$, with λ_k serving as the corresponding eigenvalue. By substituting this ansatz into the differential equation and solving for the amplitude $A_k(\Omega)$ of the response, we obtain

$$A_k(\Omega) = \frac{\sigma \cdot \mathbf{w}_k}{-\text{Re}(\lambda_k) + i(\Omega - \text{Im}(\lambda_k))}. \quad (\text{G4})$$

For each eigenvalue λ_k , we find a response amplitude that follows a Lorentzian profile, centered at $\Omega = \text{Im}(\lambda_k)$. The system's response function $\chi_{\text{rot}}(\Omega) = \sum_k A_k(\Omega)$ around the NESS resembles the response of a harmonic oscillator, with resonance frequencies $\text{Im}(\lambda_k)$ and damping rates $\text{Re}(\lambda_k)$.

Let us demonstrate for the driven damped harmonic oscillator, given by the EOMs $\ddot{x} + \omega_0 x + \gamma \dot{x} = F \cos \omega_d t$, with γ the linear damping coefficient and ω_0 the natural frequency. The system is driven with a strength F and driving frequency ω_d . Naturally, the response of the harmonic oscillator can be solved exactly. However, as we later deal with the nonlinear extension, we compute the linear response under the first order in the Floquet expansion (as performed in the main text). For this, the system is written in a rotating frame at the driving frequency $x = u \cos(\omega_d t) + v \sin(\omega_d t)$ and averaged over the period $T = \pi/\omega_d$. As such, the resulting autonomous EOMs in the rotating frame yield

$$\dot{u} = -\frac{\gamma}{2}u + \frac{\Delta}{2}v, \quad (\text{G5})$$

$$\dot{v} = -\frac{\gamma}{2}v - \frac{\Delta}{2}u - \frac{F}{2\omega_d}. \quad (\text{G6})$$

The EOMs are linear, and the drive just acts as a displacement in the rotating frame. Hence, we have a Jacobian independent of the NESS:

$$\mathcal{J} = \frac{1}{2} \begin{pmatrix} -\gamma & \Delta \\ -\Delta & -\gamma \end{pmatrix},$$

with γ the linear damping coefficient and $\Delta = (\omega_d^2 - \omega_0^2)/\omega_d$ the detuning between the natural frequency ω_0 and driving frequency ω_d . The Jacobian has two eigenvectors: $\mathbf{w}_{\pm} = \frac{1}{\sqrt{2}}(\pm i, 1)$ with eigenvalues $\lambda_{\pm} = \frac{1}{2}(-\gamma \mp \Delta)$. As expected, due to the Jacobian being real, the eigenvalues come in complex conjugate pairs. The dependence of the imaginary part of the eigenvalues on the drive frequency is shown in Fig. 10(a). The dependence is linear around the resonance condition of the drive $\omega_0 = \omega_d$, as expected for the harmonic oscillator. Hence, the imaginary part of the complex conjugate eigenvalues changes sign when the sign of the detuning Δ changes.

The response function in the rotating frame then gives $\chi_{\text{rot}}(\Omega) = A_+(\Omega) + A_-(\Omega)$. In Figs. 10(b)–10(e), we plot the real and imaginary parts of the response function separately for $\omega_d < \omega_0$ [(b) and (c)] and $\omega_d > \omega_0$ [(d) and (e)]. The real part quantifies the reactivity of the response. The larger the real part, the more the system will respond to a given probe frequency Ω . The imaginary part quantifies how much energy is absorbed or dissipated when the system interacts with an external field. In addition, the response functions are color coded by the respective contribution of the two eigenvalues $|A_+| - |A_-|$.

The imaginary part of the response function $\text{Im}(\chi_{\text{rot}})$ has two distinctive peaks at $\pm\Delta$, one for each eigenvalue. However, they have an opposite sign, indicating the resonator is emitting (λ_-) or absorbing (λ_+). Which of the two complex conjugate sidebands is the absorbing or emitting excitation is determined by the corresponding eigenvector. We can encode

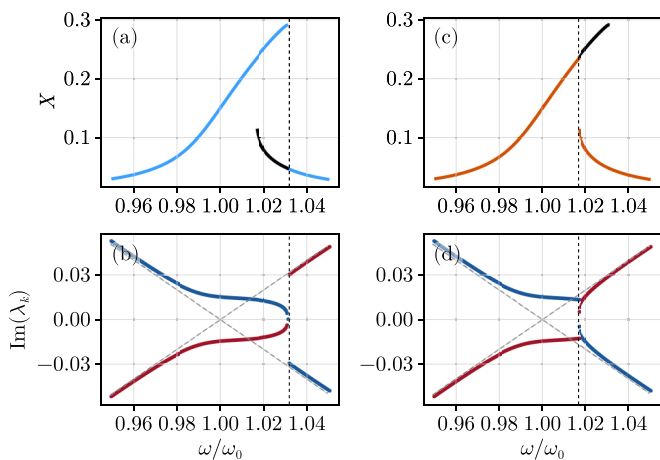


FIG. 11. Linear response of a driven damped duffing oscillator in the rotating frame. (a) Amplitude response $X = \sqrt{u^2 + v^2}$ as a function of the detuning of the up sweep undergoing a bifurcation at the vertical black dashed line. (b) Corresponding imaginary part of the eigenvalues color coded by the symplectic norm of each eigenvector, indicating the transition between absorbing and emitting responses. (c) and (d) Same as panels (a) and (b) but for the down sweep.

this in a measure, dubbed the symplectic norm [7,31,32]:

$$\begin{aligned} dS_k^2 &\equiv i[c_k^u(c_k^v)^* - (c_k^u)^*c_k^v] \\ &= 2(\text{Re}(c_k^u)\text{Im}(c_k^v) - \text{Im}(c_k^u)\text{Re}(c_k^v)), \end{aligned} \quad (\text{G7})$$

where c_k^u and c_k^v are the components of the eigenvector $\mathbf{w}_k = (c_k^u, c_k^v)$ of the Jacobian. Here, we assume that the eigenvectors are Euclidean normalized, i.e., $\|\mathbf{w}_k\|_2 = \sqrt{\mathbf{w}_k \cdot \mathbf{w}_k} = 1$. For a given eigenvector \mathbf{w}_k , the dS_k^2 can be positive or negative, indicating whether the excitation is emitting ($dS_k^2 > 0$) or absorbing ($dS_k^2 < 0$). Notice that for negative detuning $\Delta < 0$, the emitting sideband λ_+ has a positive frequency $\text{Im}(\lambda_+) =$

$-\Delta$. This reflects the fact that resonators need a frequency $-\Delta$ to excite the resonant frequency at $\omega_d + \text{Im}(\lambda_+) \approx \omega_0$. Due to our Floquet expansion, we have that $\omega_d - \Delta \approx \omega_0$ is only approximately equal. This is because the perturbation expands in a rotating frame of the driving frequency, only adding order by order the dynamics at ω_0 . As a result, the steady state of the resonator, where there is no excitation at ω_0 , is captured exactly by the expansion. Nevertheless, the linear response involves the resonant frequency ω_0 , leading to an incorrect sideband frequency. Similarly, for $\Delta > 0$, the emitting sideband λ_+ has a negative frequency $\text{Im}(\lambda_+) = -\Delta$, such that $\omega_d + \text{Im}(\lambda_+) \approx \omega_0$. Hence, the symplectic norm of the sidebands reveals whether the system is driven below or above its eigenfrequency.

We can perform a similar analysis for the Duffing resonator with the EOM $\ddot{x} + \omega_0^2 x + \gamma \dot{x} + \beta x^3 = F \cos(\omega_d t)$, where β is called the Duffing coefficient. Computing the slow-flow equations, we have

$$\dot{u} = -\frac{\gamma}{2}u + \left(\frac{\Delta}{2} - \frac{3\beta(u^2 + v^2)}{8\omega_d}\right)v, \quad (\text{G8})$$

$$\dot{v} = -\frac{\gamma}{2}v - \left(\frac{\Delta}{2} - \frac{3\beta(u^2 + v^2)}{8\omega_d}\right)u - \frac{F}{2\omega_d}, \quad (\text{G9})$$

such that the Jacobian for a NESS with phase space coordinates $\tilde{\mathbf{u}}$ reads

$$\mathcal{J} = \frac{1}{2} \begin{pmatrix} -\gamma - \frac{3\beta\tilde{u}\tilde{v}}{4\omega_d} & \Delta - \frac{3\beta(\tilde{u}^2 + 3\tilde{v}^2)}{4\omega_d} \\ -\Delta + \frac{3\beta(3\tilde{u}^2 + \tilde{v}^2)}{4\omega_d} & -\gamma + \frac{3\beta\tilde{u}\tilde{v}}{2\omega_d} \end{pmatrix}. \quad (\text{G10})$$

In contrast to the harmonic oscillator, the Duffing resonator has two different NESS solutions to Eqs. (G8) and (G9): one with high amplitude \mathbf{u}_{HI} and one with low amplitude \mathbf{u}_{LO} . We show these NESS in Figs. 11(a) and 11(c) for both an up and a down sweep, respectively. As shown, if one sweeps the drive frequency ω_d continuously around the resonance frequency ω_0 , one can bifurcate from one NESS to another, leading to a hysteresis upon inversion of the sweep direction.

The Jacobian gives the eigenvalues

$$\lambda_{\pm} = -\frac{\gamma}{2} \pm \frac{1}{8\omega_d} \sqrt{-(3\beta(\tilde{u}^2 + \tilde{v}^2) - 4\Delta\omega_d)(9\beta(\tilde{u}^2 + \tilde{v}^2) - 4\Delta\omega_d)}.$$

Naturally, they still depend on the amplitude of the NESS solutions of Eqs. (G8) and (G9). In Figs. 11(b) and 11(d), the imaginary part of the eigenvalues is shown for an up sweep and a down sweep. For small amplitude of the NESS solutions $\|\tilde{\mathbf{u}}\|^2 = \tilde{u}^2 + \tilde{v}^2 \ll 1$, the solutions behave effectively linear, indicated by the dashed gray lines. However, due to the nonlinearity, the sideband frequency renormalizes, avoiding a crossing of the sidebands at the resonance frequency $\omega_d = \omega_0$. Instead, the sidebands tend to be less influenced by the change of the drive frequency, i.e., $|\partial \text{Im}(\lambda)/\partial \omega_d| \ll 1$. Furthermore, the NESS keeps its symplectic hierarchy. In contrast to the harmonic oscillator, the system does not switch sign of the eigenvalues at $\Delta = 0$ (cf. Fig. 10). This is because the natural frequency becomes renormalized by the nonlinearity, i.e., $\tilde{\omega}_0 = \omega_0 + 3\beta((\tilde{u}^2 + \tilde{v}^2)^2)/8$, such that when the system recedes in the NESS \mathbf{u}_{HI} , the system always needs

positive $\text{Im}(\lambda)$ to excite the renormalized natural frequency ($\omega_d + \text{Im}(\lambda) \approx \tilde{\omega}_0$).

Similar to the harmonic oscillator case, pairs of an emitting and an absorbing sideband appear, indicated by the red ($dS_k^2 < 0$) and blue ($dS_k^2 > 0$) colors in Figs. 11(b) and 11(d). The bifurcation in both the up and down sweeps coincide with the resonance of the absorbing and emitting sidebands at $\text{Im}(\lambda) = 0$. The collision leads to an instability in the system where the NESS becomes unstable, also known as a saddle-node bifurcation. After the instability, the system falls into the other NESS solution. When bifurcating from one NESS to another, the amplitude of the sweep abruptly changes and therefore the natural frequency is also renormalized to $\tilde{\omega}_0$. Hence, to still fulfill $\omega_d + \text{Im}(\lambda) \approx \tilde{\omega}_0$ for the emitting eigenvalue, we need that the symplectic norm switches sign for the two eigenvalues.

3. Linear response in the laboratory frame

The PNP response in Fig. 2 is measured in the laboratory frame. Hence, we need to determine the perturbation in terms of the variables $x_i(t)$. To achieve this, we re-express the solution found for Eq. (G3) as $\delta \mathbf{u}_k = A_k(\Omega)(\mathbf{w}_k e^{i\Omega t} + \mathbf{w}_k^* e^{-i\Omega t})$. Substituting this into the ansatz from Eq. (2) and reducing the trigonometric terms, we obtain for the additional response to the probe $\delta x_i(t) = \sum_k A_k(\Omega) \delta x_{i,k}(t)$ with

$$\begin{aligned} \delta x_{i,k}(t) = & (\text{Re}(c_k^{u_i}) - \text{Im}(c_k^{v_i})) \cos((2\omega_{d,i} - \Omega)t) \\ & + (\text{Im}(c_k^{u_i}) + \text{Re}(c_k^{v_i})) \sin((2\omega_{d,i} - \Omega)t) \\ & + (\text{Re}(c_k^{u_i}) + \text{Im}(c_k^{v_i})) \cos(\Omega t) \\ & + (\text{Re}(c_k^{v_i}) - \text{Im}(c_k^{u_i})) \sin(\Omega t), \end{aligned} \quad (\text{G11})$$

where $c_k^{u_i}$ and $c_k^{v_i}$ represent the components of $\delta \mathbf{u}$ corresponding to the harmonics $\omega_{d,i}$ in the slow-flow expansion [cf. Eqs. (F9)–(F12)].

Taking the Fourier transform of $x_i(t)$ gives the linear response function in the laboratory frame $\chi(\tilde{\omega})$. Hence, the resulting PSD of the i th resonator in the laboratory frame is given by

$$|\chi_i(\tilde{\omega})|^2 = \sum_k (1 - dS_{i,k}^2) L(\tilde{\omega})_{\omega_{d,i} + \text{Im}[\lambda_k], \text{Re}[\lambda_k]}, \quad (\text{G12})$$

where $L(x)_{x_0, \gamma} = 1/((x - x_0)^2 + \gamma^2)$ is the Lorentzian distribution, and we used that $L(x)_{x_0, \gamma} = L(x + \Delta)_{x_0 + \Delta, \gamma}$. Furthermore, we have defined the conversion factor

$$dS_{i,k}^2 = 2(\text{Re}[c_k^{u_i}] \text{Im}[c_k^{v_i}] - \text{Im}[c_k^{u_i}] \text{Re}[c_k^{v_i}]). \quad (\text{G13})$$

This solution holds for each eigenvalue λ_k of the Jacobian. The linear response function $\chi[\delta x_{i,k}](\tilde{\omega})$ for each eigenvalue λ_k and harmonic $\omega_{d,i}$ consists of a Lorentzian centered at $\omega_{d,i} - \text{Im}[\lambda_k]$, with amplitude $1 + dS_{i,k}^2$, and a Lorentzian centered at $\omega_{d,i} + \text{Im}[\lambda_k]$, with amplitude $1 - dS_{i,k}^2$. Hence, the PSD of the system in the state $\tilde{\mathbf{u}}$ is fully characterized by the complex eigenvalues and eigenvectors of $\mathcal{J}(\tilde{\mathbf{u}})$. In Appendix G2, we computed that the eigenvectors $\mathbf{w}_{\pm} = \frac{1}{\sqrt{2}}(\pm i, 1)$ with eigenvalues $\lambda_{\pm} = \frac{1}{2}(-\gamma \mp \Delta)$ for the harmonic oscillator. Hence, we find that the conversion factor $\alpha_{\pm} = \mp 1$. Although in the rotating frame we have two resonant sidebands, in the laboratory frame, the $\omega_d + \text{Im}[\lambda_k]$ sideband has a zero amplitude. This results in the harmonic oscillator only having one sideband at $\omega_d - \text{Im}[\lambda_k] \approx \omega_0$ with a width of $\gamma/2$.

For the Duffing resonator, the sidebands shown in Fig. 11 can be seen in the nonrotating frame in Figs. 12(b) and 12(d). In the linear regimes discussed in Appendix G2, we have the same PSD response as the harmonic oscillator, i.e., one sideband $\omega_d + \text{Im}[\lambda_k] \approx \omega_0$ with a width of $\gamma/2$ and the other $\omega - \text{Im}[\lambda_k]$ sideband not visible due to $dS_{i,-}^2 \approx 1$. More interestingly, when the resonator has a high amplitude—and therefore is in a nonlinear regime—two sideband frequencies change linearly proportional to ω_d . The comparable intensity of the sidebands is closely related to the squeezing of the NESS due to the nonlinearity [20]. Indeed, we can define a squeezing measure as the ratio between the amplitude of the

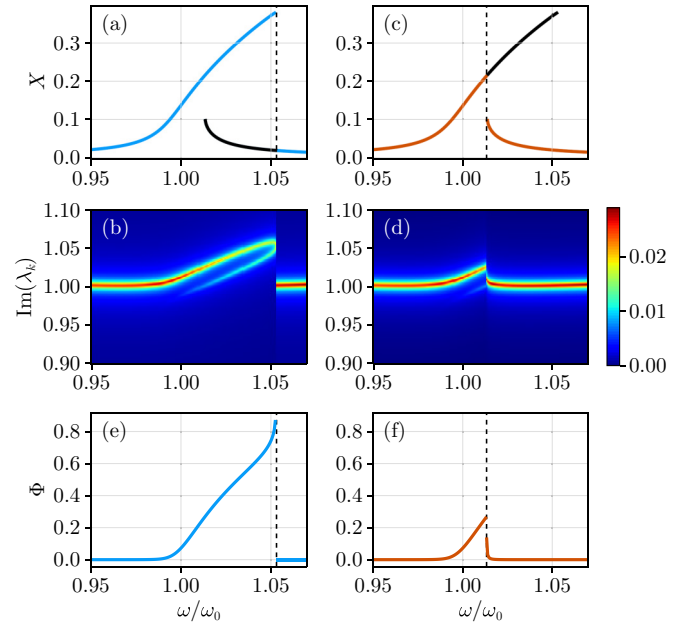


FIG. 12. Laboratory-frame linear response of a Duffing resonator. (a) Amplitude response $X = \sqrt{u^2 + v^2}$ as a function of the detuning of the up sweep undergoing a bifurcation at the vertical black dashed line. (b) Corresponding PSD generated by the probe figure illustrating the emergence of sidebands due to nonlinear dynamics, highlighting how the spectral response evolves from a single peak in the low-amplitude (linear) regime to a pair of distinct sidebands when the resonator enters the nonlinear regime. (c) Corresponding squeezing measure Eq. (G14) for the up sweep. (d)–(f) Same as panels (a)–(c) but for the down sweep.

two sidebands:

$$\Phi_{i,k} \equiv \left(\frac{1 - dS_{i,k}^2}{1 + dS_{i,k}^2} \right)^{\text{sign}(dS_{i,k}^2)}. \quad (\text{G14})$$

Here, we have to take into account the simplicity of the sidebands (cf. Appendix G2). The measure can take a value from 0 to 1, where $\Phi_{i,k} = 0$ means not squeezed and $\Phi_{i,k} = 1$ means maximally squeezed. Note that the squeezing for sideband of λ_+ is the same as λ_- . In Figs. 12(e) and 12(f), we show the squeezing measure for the up and down sweeps.

APPENDIX H: LINEAR RESPONSE THEORY OF THE MODEL

1. Jacobian

In the main text, we derived the linear response on top of the NESS to theoretically interpret the PNP measurements. This was done by linearizing the EOMs for the effective system, Eqs. (F9)–(F12), around the rotating NESS $\tilde{\mathbf{u}}$. We introduce a small perturbation $\delta \mathbf{u} = \mathbf{u} - \tilde{\mathbf{u}}$, which leads to a new set of differential equations:

$$\frac{d\mathbf{u}}{d\delta} = \mathcal{J}(\tilde{\mathbf{u}}) \delta \mathbf{u}, \quad (\text{H1})$$

where the dynamics of the perturbations are governed by the eigensystem of the 4×4 Jacobian \mathcal{J} , evaluated at $\tilde{\mathbf{u}}$.

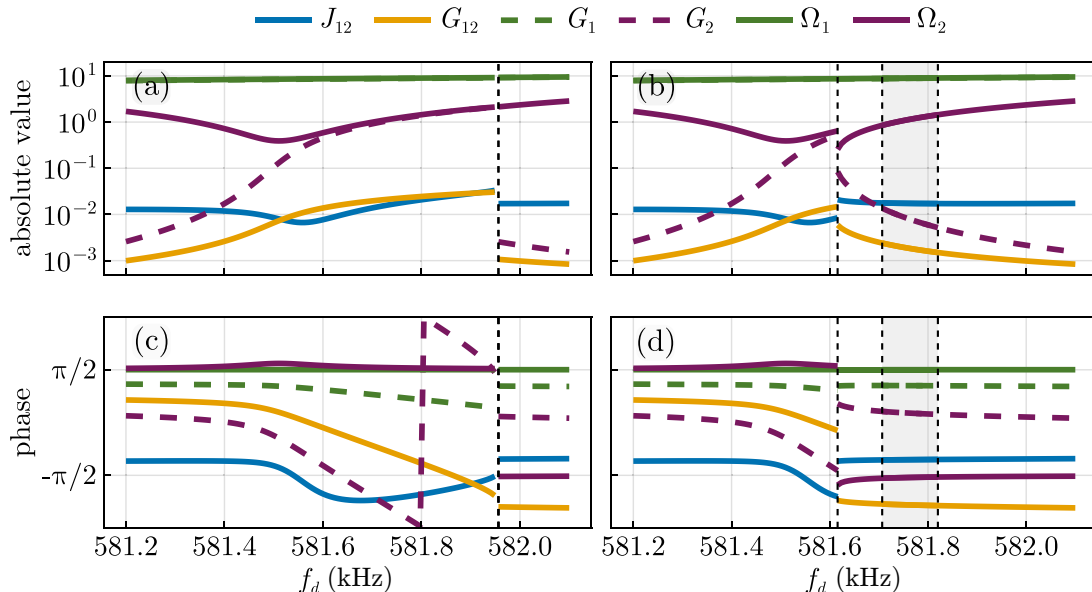


FIG. 13. Matrix elements of the dynamical matrix. (a) and (b) The absolute value of the matrix elements for the up and down sweeps, respectively. (c) and (d) The phase the matrix elements for the up and down sweeps, respectively.

The Jacobian is expressed as

$$\mathcal{J} = J + \begin{pmatrix} -\frac{\gamma_1}{2} - \frac{\eta_1}{8} Z_1^u & -\frac{\eta_1}{8} u_1 v_1 & 0 & 0 \\ -\frac{\eta_1}{8} u_1 v_1 & -\frac{\gamma_1}{2} - \frac{\eta_1}{8} Z_1^v & 0 & 0 \\ 0 & 0 & -\frac{\gamma_2}{2} - \frac{\eta_2}{8} Z_2^u & -\frac{\eta_2}{8} u_2 v_2 \\ 0 & 0 & -\frac{\eta_2}{8} u_2 v_2 & -\frac{\gamma_2}{2} - \frac{\eta_2}{8} Z_2^v \end{pmatrix}, \quad (\text{H2})$$

with

$$J = \begin{pmatrix} \frac{3(\xi u_1 v_2 - \xi u_2 v_1 + \beta_1 u_1 v_1)}{4\omega_d} & -\frac{6\xi Y_{12} + 2\zeta X_2^2 + 3\beta_1 Z_1^v}{8\omega_d} + \frac{\Delta_1}{2} & \frac{2\zeta u_2 v_1 - 3\xi u_1 v_1}{4\omega_d} & \frac{3\xi(u_1^2 - v_1^2) + 4\zeta v_1 v_2}{8\omega_d} \\ -\frac{6\xi Y_{12} + 2\zeta X_2^2 + 3\beta_1 Z_1^u}{8\omega_d} + \frac{\Delta_1}{2} & -\frac{3(\xi u_1 v_2 - \xi u_2 v_1 + \beta_1 u_1 v_1)}{4\omega_d} & -\frac{3\xi u_1^2 - 3\xi v_1^2 + 4\zeta u_1 u_2}{8\omega_d} & -\frac{u_1(3\xi v_1 + 2\zeta v_2)}{4\omega_d} \\ \frac{u_1(3\xi v_1 + 2\zeta v_2)}{12\omega_d} & \frac{3\xi(u_1^2 - v_1^2) + 4\zeta v_1 v_2}{24\omega_d} & \frac{\beta_2 u_2 v_2}{4\omega_d} & \frac{2\zeta X_1^2 + 3\beta_2 Z_2^v}{24\omega_d} + \frac{\Delta_2}{2} \\ -\frac{3\xi u_1^2 - 3\xi v_1^2 + 4\zeta u_1 u_2}{24\omega_d} & \frac{v_1(3\xi u_1 - 2\zeta u_2)}{12\omega_d} & -\frac{2\zeta X_1^2 + 3\beta_2 Z_2^u}{24\omega_d} + \frac{\Delta_2}{2} & -\frac{\beta_2 u_2 v_2}{4\omega_d} \end{pmatrix}. \quad (\text{H3})$$

Given that Eq. (H1) is a set of first-order ordinary differential equations, the system's dynamics are then determined by the exponential $e^{\lambda_k t}$, where λ_k are the eigenvalues of the Jacobian. If $\text{Re}(\lambda_k) < 0$ for all λ_k , the NESS $\bar{\mathbf{u}}$ is stable. However, if $\text{Re}(\lambda_k) > 0$ for at least one eigenvalue, the state becomes unstable, and perturbations like noise or small external drives will push the system away from $\bar{\mathbf{u}}$. The eigenvalues for the NESS for both the up and down sweeps are shown in Fig. 2.

2. Fluctuation dynamical matrix

In the main text, we introduced the matrices \mathcal{A}^n and \mathcal{B}^n , which describe frequency shifts, hopping, and single- and two-mode squeezing of fluctuations around the relevant responses at ω_d and $3\omega_d$, caused by nonlinearities. Here, we present their explicit forms:

$$\mathcal{A}^n = \begin{pmatrix} \Omega_1 & J_{12} \\ J_{12}^* & \Omega_2 \end{pmatrix}, \quad \mathcal{B}^n = \begin{pmatrix} 2G_1 & G_{12} \\ G_{12} & 2G_2 \end{pmatrix}. \quad (\text{H4})$$

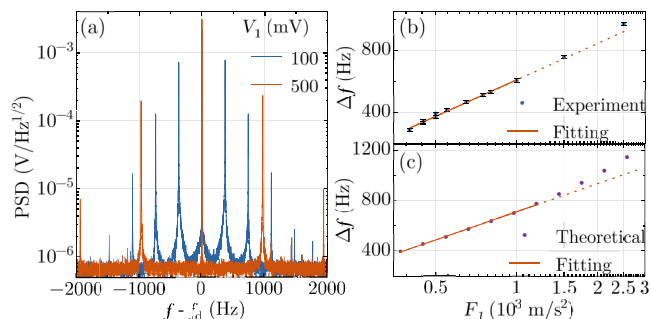


FIG. 14. (a) PNP-measured frequency spectra of the frequency comb for $V_1 = 100$ and 500 mV. The injected white noise has $V_{\text{rms}} = 100$ mV and bandwidth 2.5 MHz. (b) Measured and (c) predicted dependence of Δf on F_1 , respectively.

In Eq. (H4), the renormalized fluctuation frequencies are

$$\Omega_1 = -\frac{3i\gamma_1\omega_d^2 + \alpha_1\alpha_1^*(9\beta_1 + 3i\eta_1\omega_d) + \alpha_2\zeta\alpha_2^*}{6\omega_d^2}, \quad (\text{H5})$$

$$\Omega_2 = -\frac{3i\gamma_2\omega_d^2 + \alpha_1\zeta\alpha_1^* + \alpha_2\alpha_2^*(\beta_2 + i\eta_2\omega_d)}{6\omega_d^2}, \quad (\text{H6})$$

the hopping amplitude is

$$J_{12} = -\frac{2\alpha_1\zeta\alpha_2^* + 3\sqrt{3}\xi(\alpha_1^*)^2}{12\omega_d^2}, \quad (\text{H7})$$

and the single- and two-mode squeezing amplitudes are

$$G_1 = -\frac{3\alpha_1^2(4\beta_1 + i\eta_1\omega_d) + 8\sqrt{3}\alpha_2\xi\alpha_1^* + i\eta_1\omega_d(\alpha_1^*)^2 - 8\Delta_1\omega_d^2}{16\omega_d^2}, \quad (\text{H8})$$

$$G_2 = -\frac{\alpha_2^2(4\beta_2 + 3i\eta_2\omega_d) + i\eta_2\omega_d(\alpha_2^*)^2 - 24\Delta_2\omega_d^2}{48\omega_d^2}, \quad (\text{H9})$$

$$G_{12} = -\frac{\alpha_1\alpha_2\zeta}{2\omega_d^2}, \quad (\text{H10})$$

where $\alpha_1 = \sqrt{(\omega_d/2)}(u_1 - iv_1)$ and $\alpha_2 = \sqrt{(3\omega_d/2)}(u_2 - iv_2)$.

The dependence of these quantities for experimental parameters corresponding to Eq. (2) in the main text is shown in Fig. 13.

APPENDIX I: POWER-DEPENDENT FREQUENCY SPACING IN THE FREQUENCY COMB

We study the tunability of the frequency comb properties. The power intensity and bandwidth of the frequency combs can be tuned by adjusting ω_d , while approximately maintaining their free spectral range (i.e., spacing $\delta\omega = 2\pi\Delta f$).

During a down sweep, the PSD initially increases in the frequency range where the noise sidebands converge; see Figs. 2(c) and 2(d). The frequency comb remains stable across

a wide range of excitation power V_1 , as shown in Fig. 14(a). The free spectral range of the comb is strongly dependent on the input power, with $\Delta\omega$ showing a logarithmic dependence on the generalized force F_1 (where $F_1 \sim 10^3$ m/s² corresponds to $V_1 \sim 200$ mV by fitting of the linear and nonlinear frequency responses shown in Fig. 5), as shown in Fig. 14(b). This behavior aligns with the theoretical prediction, where Δf is derived from the fluctuations across the Hopf bifurcation [Fig. 14(c)]. This simple dependence of Δf on V_1 makes the control of Δf practical. As F_1 further increases, Δf gradually deviates from the logarithmic relationship in both experiment and theory; see Figs. 14(b) and 14(c). Besides, the intensity of the frequency comb decreases as V_1 increases. Figure 14(a) shows the frequency comb for $V_1 = 100$ mV, where it shows the highest intensity, and for 500 mV, where the intensity of the innermost sideband has decreased to about 1/4 compared to that for $V_1 = 100$ mV.

-
- [1] S. H. Strogatz, *Nonlinear Dynamics and Chaos: With Applications to Physics, Biology, Chemistry and Engineering* (Westview Press, Boca Raton, 2000).
- [2] L. Edelstein-Keshet, Limit cycles, oscillations, and excitable systems, in *Mathematical Models in Biology* (Society for Industrial and Applied Mathematics, Philadelphia, 2005), Chap. 8, pp. 311–380.
- [3] J. Guckenheimer and P. Holmes, *Nonlinear Oscillations, Dynamical Systems, and Bifurcations of Vector Fields, Applied Mathematical Sciences* (Springer, New York, 1983).
- [4] T. Faust, J. Rieger, M. J. Seitner, J. P. Kotthaus, and E. M. Weig, Coherent control of a classical nanomechanical two-level system, *Nat. Phys.* **9**, 485 (2013).
- [5] M. Frimmer and L. Novotny, The classical Bloch equations, *Am. J. Phys.* **82**, 947 (2014).
- [6] D. Halg, T. Gislser, E. C. Langman, S. Misra, O. Zilberberg, A. Schliesser, C. L. Degen, and A. Eichler, Strong parametric coupling between two ultracoherent membrane modes, *Phys. Rev. Lett.* **128**, 094301 (2022).
- [7] V. Dumont, M. Bestler, L. Catalini, G. Margiani, O. Zilberberg, and A. Eichler, Hamiltonian reconstruction via ringdown dynamics, *Phys. Rev. Res.* **6**, 043012 (2024).
- [8] G. Villa, J. del Pino, V. Dumont, G. Rastelli, M. Michałek, A. Eichler, and O. Zilberberg, Topological classification of driven-dissipative nonlinear systems, [arXiv:2406.16591](https://arxiv.org/abs/2406.16591) [cond-mat.mes-hall].
- [9] S. Hourı, D. Hatanaka, M. Asano, R. Ohta, and H. Yamaguchi, Limit cycles and bifurcations in a nonlinear mems resonator with a 1:3 internal resonance, *Appl. Phys. Lett.* **114**, 103103 (2019).
- [10] N. Carlon Zambon, S. R. K. Rodriguez, A. Lemaître, A. Harouri, L. Le Gratiet, I. Sagnes, P. St-Jean, S. Ravets, A. Amo, and J. Bloch, Parametric instability in coupled nonlinear microcavities, *Phys. Rev. A* **102**, 023526 (2020).

- [11] A. Ganesan, C. Do, and A. Seshia, Excitation of coupled phononic frequency combs via two-mode parametric three-wave mixing, *Phys. Rev. B* **97**, 014302 (2018).
- [12] M. Li and G. Haller, Nonlinear analysis of forced mechanical systems with internal resonance using spectral submanifolds, part II: Bifurcation and quasi-periodic response, *Nonlinear Dyn.* **110**, 1045 (2022).
- [13] J. del Pino, J. Kořata, and O. Zilberberg, Limit cycles as stationary states of an extended harmonic balance ansatz, *Phys. Rev. Res.* **6**, 033180 (2024).
- [14] T. W. Strganac, J. Ko, D. E. Thompson, and A. J. Kurdila, Identification and control of limit cycle oscillations in aeroelastic systems, *J. Guid. Control Dyn.* **23**, 1127 (2000).
- [15] W. Wang, Epidemic models with nonlinear infection forces, *Math. Biosci. Eng.* **3**, 267 (2006).
- [16] H.-W. Lorenz, *Nonlinear Dynamical Economics and Chaotic Motion* (Springer, Berlin, Heidelberg, 1993).
- [17] M. C. Cross and P. C. Hohenberg, Pattern formation outside of equilibrium, *Rev. Mod. Phys.* **65**, 851 (1993).
- [18] M. C. Lifshitz, R. Cross, Nonlinear dynamics of nanomechanical and micromechanical resonators, in *Reviews of Nonlinear Dynamics and Complexity* (Wiley-VCH, Weinheim, 2009), pp. 1–52.
- [19] M. Poot and H. S. van der Zant, Mechanical systems in the quantum regime, *Phys. Rep.* **511**, 273 (2012).
- [20] J. S. Huber, G. Rastelli, M. J. Seitner, J. Kölbl, W. Belzig, M. I. Dykman, and E. M. Weig, Spectral evidence of squeezing of a weakly damped driven nanomechanical mode, *Phys. Rev. X* **10**, 021066 (2020).
- [21] F. Yang, M. Fu, B. Bosnjak, R. H. Blick, Y. Jiang, and E. Scheer, Mechanically modulated sideband and squeezing effects of membrane resonators, *Phys. Rev. Lett.* **127**, 184301 (2021).
- [22] J. del Pino, J. J. Slim, and E. Verhagen, Non-Hermitian chiral phononics through optomechanically induced squeezing, *Nature (London)* **606**, 82 (2022).
- [23] T. L. Heugel, A. Eichler, R. Chitra, and O. Zilberberg, The role of fluctuations in quantum and classical time crystals, *SciPost Phys. Core* **6**, 053 (2023).
- [24] A. Eichler and O. Zilberberg, *Classical and Quantum Parametric Phenomena* (Oxford University Press, Oxford, 2023).
- [25] F. Yang, R. Waitz, M. Fu, and E. Scheer, Quantitative signal extraction in the dynamic range of nanomechanical systems by free and constrained fitting, *Sens. Actuators A: Phys.* **354**, 114307 (2023).
- [26] R. Waitz, S. Nöbner, M. Hertkorn, O. Schecker, and E. Scheer, Mode shape and dispersion relation of bending waves in thin silicon membranes, *Phys. Rev. B* **85**, 035324 (2012).
- [27] R. Waitz, C. Lutz, S. Nöbner, M. Hertkorn, and E. Scheer, Spatially resolved measurement of the stress tensor in thin membranes using bending waves, *Phys. Rev. Appl.* **3**, 044002 (2015).
- [28] M. J. Seitner, M. Abdi, A. Ridolfo, M. J. Hartmann, and E. M. Weig, Parametric oscillation, frequency mixing, and injection locking of strongly coupled nanomechanical resonator modes, *Phys. Rev. Lett.* **118**, 254301 (2017).
- [29] A. H. Nayfeh and D. T. Mook, *Nonlinear Oscillations* (John Wiley & Sons, New York, 1995).
- [30] J. Kořata, J. del Pino, T. L. Heugel, and O. Zilberberg, HarmonicBalance.jl: A Julia suite for nonlinear dynamics using harmonic balance, *SciPost Phys. Codebases* **6** (2022).
- [31] M. Soriente, R. Chitra, and O. Zilberberg, Distinguishing phases using the dynamical response of driven-dissipative light-matter systems, *Phys. Rev. A* **101**, 023823 (2020).
- [32] M. Soriente, T. L. Heugel, K. Omiya, R. Chitra, and O. Zilberberg, Distinctive class of dissipation-induced phase transitions and their universal characteristics, *Phys. Rev. Res.* **3**, 023100 (2021).
- [33] F. Fani Sani, I. C. Rodrigues, D. Bothner, and G. A. Steele, Level attraction and idler resonance in a strongly driven Josephson cavity, *Phys. Rev. Res.* **3**, 043111 (2021).
- [34] T. Faust, J. Rieger, M. J. Seitner, P. Krenn, J. P. Kotthaus, and E. M. Weig, Nonadiabatic dynamics of two strongly coupled nanomechanical resonator modes, *Phys. Rev. Lett.* **109**, 037205 (2012).
- [35] I. Mahboob, K. Nishiguchi, H. Okamoto, and H. Yamaguchi, Phonon-cavity electromechanics, *Nat. Phys.* **8**, 387 (2012).
- [36] J. P. Mathew, J. del Pino, and E. Verhagen, Synthetic gauge fields for phonon transport in a nano-optomechanical system, *Nat. Nanotechnol.* **15**, 198 (2020).
- [37] J. Ma, X. Xi, Y. Li, and X. Sun, Nanomechanical topological insulators with an auxiliary orbital degree of freedom, *Nat. Nanotechnol.* **16**, 576 (2021).
- [38] M. Dykman, *Fluctuating Nonlinear Oscillators* (Oxford University Press, Oxford, 2012).
- [39] N. R. Bernier, L. D. Tóth, A. K. Feofanov, and T. J. Kippenberg, Level attraction in a microwave optomechanical circuit, *Phys. Rev. A* **98**, 023841 (2018).
- [40] N. R. Bernier, E. G. Dalla Torre, and E. Demler, Unstable avoided crossing in coupled spinor condensates, *Phys. Rev. Lett.* **113**, 065303 (2014).
- [41] S. Aldana, C. Bruder, and A. Nunnenkamp, Equivalence between an optomechanical system and a Kerr medium, *Phys. Rev. A* **88**, 043826 (2013).
- [42] G. A. Peterson, S. Kotler, F. Lecocq, K. Cicak, X. Y. Jin, R. W. Simmonds, J. Aumentado, and J. D. Teufel, Ultrastrong parametric coupling between a superconducting cavity and a mechanical resonator, *Phys. Rev. Lett.* **123**, 247701 (2019).
- [43] P. Forn-Díaz, L. Lamata, E. Rico, J. Kono, and E. Solano, Ultrastrong coupling regimes of light-matter interaction, *Rev. Mod. Phys.* **91**, 025005 (2019).
- [44] L. Catalini, M. Rossi, E. C. Langman, and A. Schliesser, Modeling and observation of nonlinear damping in dissipation-diluted nanomechanical resonators, *Phys. Rev. Lett.* **126**, 174101 (2021).
- [45] J. Kořata, Spatial and temporal mode engineering in nonlinear media, Ph.D. thesis, ETH Zurich, 2022.
- [46] L. D. Landau, L. Pitaevskii, A. M. Kosevich, and E. M. Lifshitz, *Theory of Elasticity, Course of Theoretical Physics*, 3rd ed. (Elsevier, Oxford, 1986), Vol. 7.
- [47] A. C. Ugural, *Plates and Shells: Theory and Analysis* (CRC Press, Boca Raton, FL, 2017).
- [48] P. Breiding and S. Timme, HomotopyContinuation.jl: A package for homotopy continuation in Julia, in *International Congress on Mathematical Software* (Springer, Cham, 2018), pp. 458–465.